Molecular Catalysis 545 (2023) 113222

Contents lists available at ScienceDirect

Molecular Catalysis

journal homepage: www.journals.elsevier.com/molecular-catalysis

Synthesis of Ru, Ni and Fe supported graphene nanoplatelets catalysts for hydrogenation of glucose into sorbitol

Nadzeya Kryvutsa [a], Pierre Eloy [b], Benoit Hackens [c], Sophie Hermans [a,*]

[a] IMCN Institute, MOST Division, UCLouvain, Place Louis Pasteur 1, Louvain-la-Neuve B-1348, Belgium
[b] IMCN Institute, BSMA Division, UCLouvain, Place Louis Pasteur 1, Louvain-la-Neuve B-1348, Belgium
[c] IMCN Institute, NAPS Division, UCLouvain, Chemin du Cyclotron 2, Louvain-la-Neuve B-1348, Belgium

ARTICLE INFO

Keywords:
Non-covalent functionalization
Graphene nanoplatelets
Non-noble metals
Glucose
Hydrogenation

ABSTRACT

Non-covalent method of graphene nanoplatelets' functionalization using the pyrene-tagged Ru, Ni and Fe precursors developed in this work offers an easy way to prepare bimetallic catalysts with different metal ratio and different compositions as Ni-Ru, Fe-Ru and Ni-Fe. First, four different metallic precursors were synthetized: Ni (0), Ni (II), Fe and Ru. Then, 16 different catalysts were prepared and fully characterized by ICP, XPS, XRD and TEM. All catalysts were then tested in the catalytic reaction of the hydrogenation of glucose into sorbitol. The ruthenium supported catalyst with 2.23 wt% shows a good conversion (66%) of glucose and high sorbitol selectivity (74%) at 160 °C under 30 bar H_2 pressure during 2 h. The non-noble metallic catalysts Ni and Fe show very low conversion and selectivity. However, the combination of these two metals shows good results: 58% of glucose conversion and 40% of sorbitol selectivity obtained with 4.12 wt% in both metals.

1. Introduction

Graphene has been intensively studied since its discovery and its isolation as a single sheet in 2004 [1]. Graphene is an all-carbon material used in many applications such as electronics, energy storage, solar cells and super capacitors [2], owing to its high surface area and advantageous thermal, electrical and mechanical properties [3–5]. Its 2D nature combined with ultrahigh thermal and electronic conductivity makes it a very good carbon support for catalysis [6], in addition to high chemical stability of carbonaceous materials in general. Graphene has attracted enormous interest especially in heterogeneous catalysis because of its extremely large surface-to-volume ratio, charge carrier mobility and functionalization ability [7]. It ideally consists of carbon atoms linked through sp^2 hybridized atomic orbitals but due to the possible presence of surface functional groups such as hydroxyl, carbonyl, carboxyl and epoxy, some sp^3-bonded carbon atoms can also be present. Principal forms of graphene used in heterogeneous catalysis are graphene oxide (GO), reduced graphene oxide (rGO), few layer graphene (FLG), multilayer graphene (MLG) and graphene nanoplatelets (GNPs) [8]. Graphene nanoplatelets with a thickness of no more than 10 layers and low density of defects, are an important part of graphene family. They retain the high thermal and electrical conductivity, with a reduced cost and high mechanical strength, all benefits for possible industrialization. Chemical functionalization of GNPs can bring new properties by introducing new organic functional groups or metallic entities on its surface. Chemical functionalization can be divided into two approaches: covalent and non-covalent [9]. Covalent functionalization provides a stable connection between GNPs and the functional groups due to covalent bonds, but it also tunes the aromatic character of graphene. Indeed, the creation of a new covalent bond with a surface carbon atom modifies its hybridization from sp^2 to sp^3 which can lead to a partial or total loss of the electronic properties of GNPs [10]. As for non-covalent functionalization, it can be achieved primarily with π-π stacking interactions. The large π system of GNPs is used as ideal scaffold for this type of functionalization with adsorbate molecules of aromatic character. New functionalities can therefore be introduced on the surface of GNPs without altering graphene's network and aromatic character [10]. The smallest entity that adopts the π-π parallel stacking configuration with graphene is pyrene [11]. This moiety was therefore selected here to optimize the immobilization of metals on GNPs in view of its application in heterogeneous catalysis.

Sorbitol was identified by the U.S. Department of Energy as one of the 12 most important value-added chemicals obtainable from biomass [12,13]. It can be potentially used as a source of alkanes for liquid

* Corresponding author.
E-mail address: sophie.hermans@uclouvain.be (S. Hermans).

https://doi.org/10.1016/j.mcat.2023.113222
Received 22 January 2023; Received in revised form 16 April 2023; Accepted 2 May 2023
Available online 9 May 2023

biofuels or as an "outstanding building block" for commodity chemicals [14]. Moreover, it can be used as additive in food, cosmetics and paper industries. Industrially, sorbitol is produced either via biochemical methods, such as conventional fermentation by *Zymomonas mobilis* or by chemical routes such as catalytic hydrogenation of glucose [15] (Fig. 1).

Non-noble (Fe, Co, Ni) and noble (Ru, Pt, Pd) metals have been used as active phases in the reaction of hydrogenation of glucose [16–19]. Nickel based catalysts (Raney type) are used due to their low cost and moderate catalytic activity, but their drawbacks are deactivation of catalyst, leaching of the active nickel and sintering. Due to leaching and dissolution of nickel during the hydrogenation, the purification of sorbitol is required at the end of the reaction, especially for food industry applications, which renders the process economically less attractive [16]. Studies of the use of ruthenium as active metal show that it is more (20 - 50 times) efficient than nickel, and ruthenium is stable against leaching, but it is much more costly [20]. The price can be reduced by supporting the metal active phase as small nanoparticles on an inert carrier. However, Raney Nickel remains the most used catalyst in the industry for this transformation. It has been reported to be enhanced by promoters like molybdenum, chromium, and iron [20–22]. Among them, Fe promoted Raney Nickel catalyst exhibits the highest reaction rate [21]. So, Fe as a promoter can maximally enhance the activity of Ni as it was also shown recently by us for supported catalysts [23]. As another option, introduction of noble metals such as Ru, Pt, Pd into Ni-based supported catalysts enhances their catalytic activity even at low loading of noble metals (Ni-Ru = 3:0.4 wt%), as shown by Ribeiro et al. [17]. The promoter effect of Ru over the Ni catalysts shows up by decreasing the reduction temperature of activated carbon supported nickel, which confirms an intimate contact between both metals [17]. The preparation method and metal concentration are very important in catalytic systems. Different synthetic methods lead to core-shell, alloy and porous structures that present different catalytic activities [24].

In this work, we report the synthesis of pyrene-tagged Ru, Ni and Fe precursors for non-covalent functionalization of GNPs. This type of functionalization allows us to introduce new functionalities and metal contents on the surface of graphene without altering its aromatic character. Moreover, the metallic composition of the catalysts can be easily tuned and the deposited molecular precursors are transformed into the active nanoparticles by gentle heating. The prepared catalysts supported on GNPs are then tested in the catalytic reaction of glucose hydrogenation either in monometallic or in bimetallic forms, allowing to highlight higher catalytic activity for the bimetallic formulations.

2. Experimental section

2.1. Materials and reagents

All manipulations were carried out under an inert atmosphere by using standard Schlenk techniques with anhydrous solvents. Hexane, tetrahydrofuran, diethyl ether, dichloromethane were distilled over sodium under nitrogen atmosphere. The graphene nanoplatelets (GNPs C750) were purchased from Sigma-Aldrich (see characteristics in Annex, Electronic Supplementary Information). Chlorodiphenylphosphine (98% Acros Organics stored under nitrogen), 4-bromobenzonitrile (99% Alfa Aesar), nBuLi (1.6 M in hexanes Sigma-Aldrich), lithium tetrahydroaluminate (95% Sigma Aldrich), N—N'-dicycolhexylcarbodiimide (99%), 4-dimethylaminopyridine (99% Sigma Aldrich), pyrenebutyric acid (95% Alfa Aesar), triruthenium dodecacarbonyl (99% Alfa Aesar), nickel (II) acetate tetrahydrate (Sigma Aldrich), bis(1,5-cycloctadiene) nickel (0) (96% Alfa Aesar) and iron pentacarbonyl (99.9% Sigma Aldrich) were used as received.

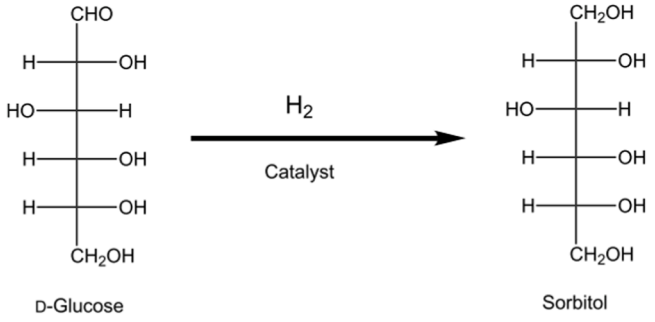

Fig. 1. Hydrogenation of glucose into sorbitol [16].

2.2. Synthesis of bifunctional ligand 6 [25]

The synthesis of compounds **3** and **4**, have been described previously [26]. In a 50 ml Schlenk flask, 1 g (1 eq., 3.4 mmol) of 4-diphenylphosphanylbenzylamine is dissolved in 20 ml of distilled dichloromethane. A solution of pyrene butyric acid (1.186 g, 1.2 eq., 4.12 mmol) is added. Then, 0.78 g (1.1 eq., 3.7 mmol) of N, N'-dicyclohexylcarbodiimide and 0.125 g (0.3 eq., 1.02 mmol) of 4-dimethylaminopyridine are added, and the mixture is stirred overnight at room temperature. The solution is washed successively two times with water, HCl (1 M), HCl (0.1 M), water, NaOH (1 M), NaOH (0.1 M), water and dried over $MgSO_4$. The crude product is purified by column chromatography (dichloromethane/ethyl acetate: 95/5) A white solid is isolated. Experimental yield: 66% ^{1}H NMR (300 MHz, CDCl3), δ (ppm): 8.28 (d, J = 9.3 Hz, 1H), 8.20–7.94 (m, 7H), 7.83 (d, J = 7.8 Hz, 1H), 7.38–7.18 (m, 14 H), 5.64 (s, 1H), 4.43 (d, J = 5.7 Hz, 2H), 3.40 (t, J = 7.1 Hz, 2H), 2.36–2.17 (m, 4H); ^{13}C NMR (75 MHz, CDCl3), δ (ppm): 172.60, 138.91, 135.62, 134.16, 133.90, 133.73, 133.48, 131.29, 130.77, 129.83, 128.80, 128.53, 128.44, 127.85, 127.38, 127.33, 127.26, 126.65, 125.79, 124.86, 124.72, 123.25, 43.19, 35.69, 32.57, 27.30; ^{31}P NMR (121 MHz, CDCl3), δ (ppm): −6.07; HRMS (ESI): *m/z* calculated for $C_{39}H_{33}ONP+H^+$: 562.22943; found: 562.22979

2.3. Synthesis of ruthenium compound 7

In a 50 ml Schlenk flask, 50 mg (1 eq., 0.078 mmol) of triruthenium dodecacarbonyl ($Ru_3(CO)_{12}$) is dissolved in 15 ml of distilled dichloromethane. 44 mg (1 eq., 0.078 mmol) of the synthetized pyrene bifunctional ligand suspended in 5 ml of DCM are added. The mixture is stirred 12 h and then concentrated under reduced pressure without heating. Basic silica gel chromatography (dichloromethane/ethyl acetate, 80/20) allowed the isolation of a dark red solid. Experimental yield: 20%; IR (ν_{CO} cm^{-1} CH_2Cl_2):1979, 1968; ^{31}P NMR (121 MHz, $CDCl_3$), δ (ppm): 37.05; HRMS (ESI): *m/z* calculated for [M-9CO+Na$^+$] calculated 2010.37, found: 2011.33.

2.4. Synthesis of nickel (II) compound 9

In a 25 ml round-bottomed flask equipped with a reflux condenser, 0.1 g (1 eq., 0.4 mmol) of nickel (II) acetate tetrahydrate is dissolved in 15 ml of the solvent: methanol/ water (90/10). To this mixture, 0.23 g (2 eq., 0.8 mmol) of the pyrene butyric acid are added. The resulting mixture is heated under reflux during 2 h. The mixture is then cooled down to room temperature. The solution is filtered and the filtrate is concentrated in vacuo to give a yellow solid. Experimental yield: 50%; IR (film, cm^{-1}): 1698 (C = O), 1407 (C = O), 837, 826, 757, 692; HRMS -ESI: *m/z* calculated for [M-H^+] $C_{40}H_{31}O_4Ni$ 633.1654; found: 633.1503

2.5. Synthesis of nickel (0) compound 11

In a 25 ml Schlenk flask 100 mg of $Ni(cod)_2$ (0.36 mmol, 1 eq.) and 400 mg of synthetized bifunctional pyrene ligand **6** (0.727 mmol, 2 eq.) were introduced, then 15 ml of distilled THF were added. The mixture was cooled down to −30 °C and stirred during 1 h. The bath was then removed and CO (1 bar) was bubbled in the flask during one hour. The

reaction was left to stir during 2 h. After removal of solvent under vacuum, the sticky brown solid was washed with cold pentane (−30 °C) and then dissolved in cold DCM (−30 °C). DCM was evaporated to form a yellow solid. Experimental yield: 39%; ^{31}P NMR (121 MHz, $CDCl_3$): 32.24, 30.73, 28.87; IR (ν_{CO} cm^{-1} CH_2Cl_2): 2069, 1999, 1938.

2.6. Synthesis of iron compound 13

In a 25 ml Schlenk flask equipped with a reflux condenser, 17 mg (0.09 mmol, 1 eq.) of $Fe(CO)_5$ are dissolved in a solution of 0.01 g (0.18 mmol, 2 eq.) of KOH in 10 ml of absolute degassed ethanol. The mixture is stirred during 1 h. 0.1 g (2 eq.) of the synthetized bifunctional ligand are then added. The resulting mixture is heated under reflux during 24 h. The mixture is then cooled down and filtered through a frit. The yellow isolated solid is washed with ethanol, water and ethanol again and then dissolved in dichloromethane. The solution is filtered, dried over Na_2SO_4 and the solvent is evaporated under reduced pressure to form a brown solid. Experimental yield: 40%; ^{31}P NMR (121 MHz, $CDCl_3$), δ (ppm): 82.45; IR (ν_{CO} cm^{-1} CH_2Cl_2): 1876; HRMS-ESI: *m/z* calculated for $C_{83}H_{68}N_2O_5P_2Fe$ 1262.640; found: 1262.3634

2.7. Catalysts preparation

The synthesis of Ru, Fe and Ni nanoparticles supported on graphene is realized by wet impregnation method. In a typical procedure, 100 mg GNPs are suspended in 30 ml dichloromethane and sonicated during 45 min. The quantity (as specified in Table S2, in Supporting information) of metallic precursor is calculated so as to obtain 3 wt.% of metal loading in the case of ruthenium and 10 wt.% in the case of nickel and iron catalysts. The metallic precursors are dissolved in 1 ml of dichloromethane and added to GNPs, the mixture is then stirred during one hour at room temperature to allow for π-π interactions to take place. The functionalized GNPs are then filtered through PVDF 0.45 μm membranes. The resulting material is thermally heated under inert atmosphere (Ar/H_2 95/5) in a tubular oven STP 16/450 from a CARBOLITE at the set temperature (400 °C or 600 °C, as specified in each case in 'Results' part) during one hour after heating ramp at 100 °C/h.

2.8. Characterization methods

NMR spectra were recorded on a Bruker spectrometer (300 MHz for ^{1}H, 75 MHz for ^{13}C, 121 MHz for ^{31}P). Chemical shifts are reported in δ (ppm) from $CDCl_3$/tetramethylsilane with solvent resonance as the internal standard for ^{1}H NMR and ^{13}C NMR, while PCl_5 was used as internal standard for ^{31}P NMR.

IR spectra were recorded on a Spectrum Two FT-IR from Perkin Elmer. Solid samples were dissolved in dichloromethane and analyzed between 4000 cm^{-1} and 750 cm^{-1}.

HRMS-ESI were recorded on a Q-Exactive orbitrap from Thermo-Fisher. Samples were ionized by direct introduction in the positive mode, as provided in the ESI.

XPS analyses were carried out at room temperature with a SSI-Xprobe (SSX 100/206) photoelectron spectrometer from Surface Science Instruments (USA), equipped with a monochromatized micro-focus Al X-ray source. Samples were stuck onto small sample holders with double face adhesive tape and then placed on an insulating ceramic carousel (Macor®, Switzerland). Charge effects were avoided by placing a nickel grid above the samples and using a flood gun set at 8 eV. The binding energies were calculated with respect to the C-(C, H) component of the C1s peak fixed at 284.4 eV. Data treatment was performed using the CasaXPS program (Casa Software Ltd., UK). The peaks were decomposed into a sum of Gaussian/Lorentzian (85/15) after subtraction of a Shirley-type baseline.

ICP analyses for determining the metal contents in solid samples were realized by MEDAC Ltd. (U.K., www.medacltd.com). The catalysts samples were digested with nitric acid on a hot plate, with hydrogen peroxide as an oxidizing agent, then made up to volume with ultrapure water (18.2Mohm water) and analyzed by ICP-OES method.

TEM images were obtained on a LEO 922 Omega Energy Filter Transmission Electron Microscope operating at 120 kV. The samples were suspended in hexane under ultrasonic treatment. One drop of suspension was deposited on holey carbon film supported on a copper grid (Holey Carbon Film 300 Mesh Cu from Electron Microscopy Sciences), which was let to dry overnight under a fumehood at room temperature before imaging.

XRD diffraction patterns were recorded with a D8-Advance diffractometer (Bruker, Germany) using Brag Brentano geometry. Diffractograms were taken between 5° and 80° (2θ) with a step size of 0.015° (2θ). The reference databases COD and PDF-2 2004 were used to match experimental peaks and identify crystalline phases.

The texture of the starting GNPs was characterized by nitrogen adsorption–desorption isotherms. The measurement was achieved by using a Micromeritics ASAP 2020 analyzer at 77 K. Before analysis, the sample was degassed for several hours at 200 °C under 4 μmmHg pressure. The analysis of the isotherms provided the specific surface area calculated with the Brunauer–Emmett–Teller (BET) equation, S_{BET}. The pore sizes were calculated using the Barrett-Joyner-Halanda (BJH) model.

2.9. Catalytic tests

Hydrogenation of D-glucose was performed in a 300 ml stainless-steel high-pressure Parr autoclave. 500 mg of glucose was added to 60 mg of catalyst in 120 ml of milli-Q water. The reactor was purged with N_2 three times to remove air. The reaction mixture was then heated at 160 °C, the autoclave was filled to a constant H_2 (>99.99% pure) pressure and reaction started (stirring was set at 1700 rpm). At the end of the reaction, the mixture was cooled down to room temperature and the solution was filtrated. The filtrate was diluted to 250 ml with milli-Q water and analyzed by HPLC. The catalyst is recovered, washed with milli-Q water and dried overnight for characterization after the catalytic run.

Standard tests to check for absence of diffusional limitations were carried out. Given the fact that graphene nanoplatelets are non-porous in nature (see Annex in Supplementary Information with characteristics of starting GNPs), internal diffusion is not problematic here.

HPLC analyses were performed with a Waters system equipped with Waters 2414 refractive index (RI) detector. An Aminex HPX 87C carbohydrate column was used, with ultrapure water as mobile phase at a flow rate of 0.5 cm^3min^{-1}, a column temperature of 30 °C and 25 μl of injected volume.

The conversion of glucose was calculated as follows: Conversion (%) $= \frac{n\ glucose\ converted}{n\ glucose\ engaged} x100$

The selectivity in sorbitol was calculated as follows: Selectivity (%) $= \frac{n\ sorbitol\ producted}{n\ glucose\ converted} x100$

The yield of sorbitol was calculated as follows: Yield (%) $= \frac{n\ sorbitol\ produced}{n\ glucose\ engaged} x100$

3. Results and discussion

The experimental strategy we followed involved several steps. First of all, a pyrene bifunctional ligand was synthesized and complexed to four metallic entities, namely Ru, Ni (II), Ni (0) and Fe. These compounds were then dispersed on the surface of the GNPs and thermally activated, to keep only the metallic cores without organic part on the surface of GNPs. The so-prepared nanoparticle catalysts were then used in catalytic tests either separately or in bimetallic combinations: Ni-Ru, Fe-Ru and Ni-Fe. The results obtained in each step will be discussed in detail below in subsequent sections.

3.1. Synthesis of the bifunctional ligand and its characterization

The phosphine ligand **6** bearing a pyrene entity was first synthesized following the synthetic route shown in Fig. 2 [25].

A halogen/lithium exchange between 4-bromobenzonitrile **2** and nBuLi followed by reaction with chlorodiphenylphosphine **1** gives the intermediate **3**. $LiAlH_4$ reduction of the nitrile group in compound **3** yielded the corresponding amine **4**, which was finally coupled with 1-pyrenebutyric acid **5** to give the bifunctional ligand **6** with an overall yield of 66%. This air-stable yellow solid **6** was fully characterized. ^1H NMR confirms the presence of aromatic entity. ^{31}P NMR peak at −6 ppm confirms that phosphorus atom is not oxidized and the mass spectra found 562.23 *m/z* for ($M + H^+$) corresponds to the theoretical pseudo-molecular ion (Supporting information Figs. S1–S4).

3.2. Synthesis of metallic (ruthenium, nickel and iron) precursors and their characterization

Four metallic precursors were synthetized (Ru, Ni (II), Ni (0), Fe). In the case of Ru, triruthenium dodecacarbonyl, $Ru_3(CO)_{12}$, was used in the synthesis. This cluster is known to give a mixture of different products during reactions of CO exchange [27–29]. $Ru_3(CO)_{12}$ was dissolved in dichloromethane and bifunctional ligand **6** was added in stoichiometric quantities (Fig. 3).

The reaction was followed by TLC and IR. The initially yellow solution ($Ru_3(CO)_{12}$ in CH_2Cl_2) becomes red within 3 h of reaction. Three more spots appear on TLC, besides the spot of the starting material. We suggest the formation of several substitution products, mono-substituted $Ru_3(CO)_{11}(PPh_2R)$, di-substituted $Ru_3(CO)_{10}(PPh_2R)_2$ and tri-substituted $Ru_3(CO)_9(PPh_2R)_3$ compounds. In the IR spectra we observe a mixture of different products (Fig. 4, orange curve). The major tri-substituted product **7** is easily identified due to its red color. It is isolated by column chromatography. The obtained purified product is a red solid stable in the air. The IR spectra (Fig. 4, blue curve) of the carbonyl region shows, as expected, a shift of the CO stretching bands to smaller wavenumber (1977 cm^{-1}, 1968 cm^{-1}), indicating the weakening of the CO bonds due to replacement of several COs by a less π-acceptor phosphine ligand.

The ^{31}P and ^1H NMR spectra were recorded in $CDCl_3$ after the purification step (Figs. S5 and S6). The position of the peak was shifted downfield (δ = 37.05 ppm) compared to the phosphine ligand at the beginning (δ = −6.07 ppm). A downfield shift in the ^{31}P resonance of the compounds is related to the π accepting ability of phosphines from the metal. The back donation of electron density from the metal towards phosphine occurs, resulting in a deshielding effect at the phosphorus atom [30]. The presence of only one phosphorus peak indicates that ruthenium bears phosphine ligands and that all of them are equivalent. The ^1H NMR also gives information about the product and shows that the phosphine ligand with pyrene was successfully added to the ruthenium cluster (Fig. S5). As for HRMS, we observe the peak of the whole tri-substituted product, including ruthenium cluster core (Ru3), three phosphine ligands and nine CO ligands (found *m/z* 2011.33) (Fig. S7).

Two different nickel precursors were then synthetized. The first one is obtained by the exchange between nickel (II) acetate and 1-pyrenebutyric acid; and the other one, by the exchange between the synthetized bifunctional ligand **6** and bis(1,5-cyclooctadiene) nickel (0), $Ni(cod)_2$, in presence of 1 bar of CO.

As for the first synthesis, nickel (II) acetate tetrahydrate **8** was used as starting reagent rather than a carbonyl cluster with a zero-oxidation state of the metal. Therefore, the commercial 1-pyrenebutyric acid **5** was used as ligand in the reaction rather than the bifunctional synthesized ligand **6** (see Fig. 1). In consequence, this reaction cannot be followed by analyzing the shifts of CO stretching bands but rather by looking at carboxylate characteristic peaks. Nickel acetate tetrahydrate **8** is known [20] as an octahedral compound: the metal center is coordinated by four oxygen atoms of water molecules and two oxygen atoms of the acetate ligand in unidentate coordination mode. However, we observe a difference Δ smaller than 200 cm^{-1} between the asymmetric (ν_{asym} = 1505 cm^{-1}) and symmetrical (ν_{sym} = 1416 cm^{-1}) carboxyl stretching frequencies in the IR spectrum of this starting material (Fig. S8), while it is usually more than 200 cm^{-1} for unidentate coordination mode. The reason for this is that the acetate oxygen that is not coordinated with the metal makes hydrogen bridges (Fig. 5) with the neighboring ligands, giving a "pseudo-bridging" arrangement [31,32].

When our starting nickel acetate compound **8** is placed in the presence of 1-pyrenebutyric acid **5**, the desired ligand-exchange reaction shown in Fig. 4 takes place, leading to the formation of product **9**. The mass spectrum (Fig. S9), *m/z* = 633.15, indicates that the product obtained is not hydrated. No band is observed in the IR spectra (Fig. S10) in the region 3600 cm^{-1} to 3400 cm^{-1}, which confirms the absence of O—H stretching vibrations. There is a strong band at 1700 cm^{-1} which is the region of C = O stretching, we observe also a band at 1205 cm^{-1} for the region of C—O stretching, and there are also CO_{asym} and CO_{sym} at 1568cm^{-1} and 1432 cm^{-1}, respectively. So, we assume that the acetates

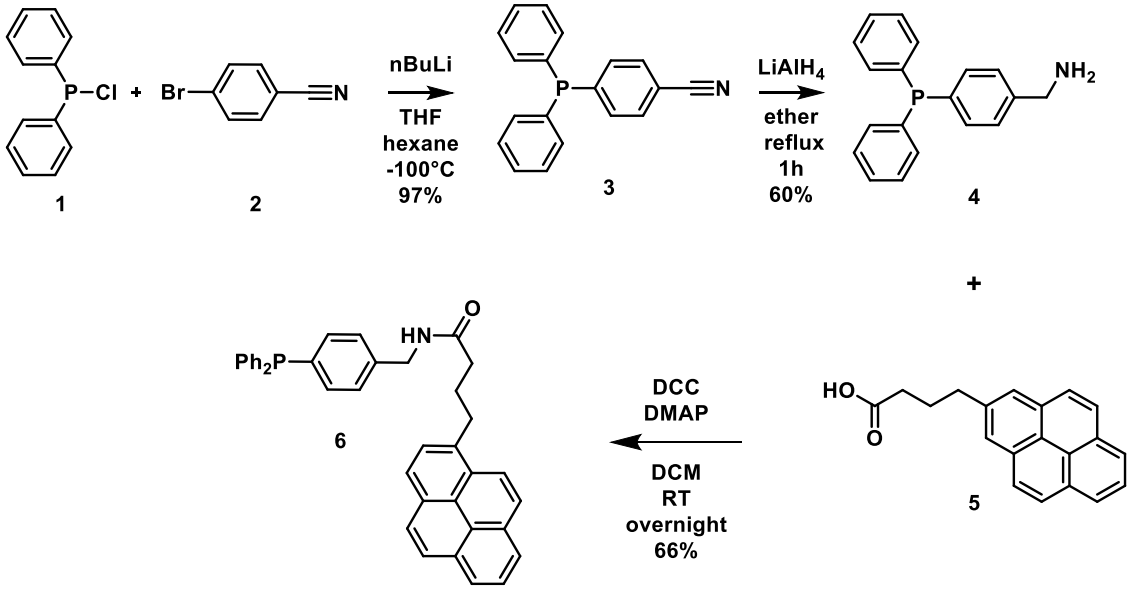

Fig. 2. Synthetic pathway of bifunctional ligand 6.

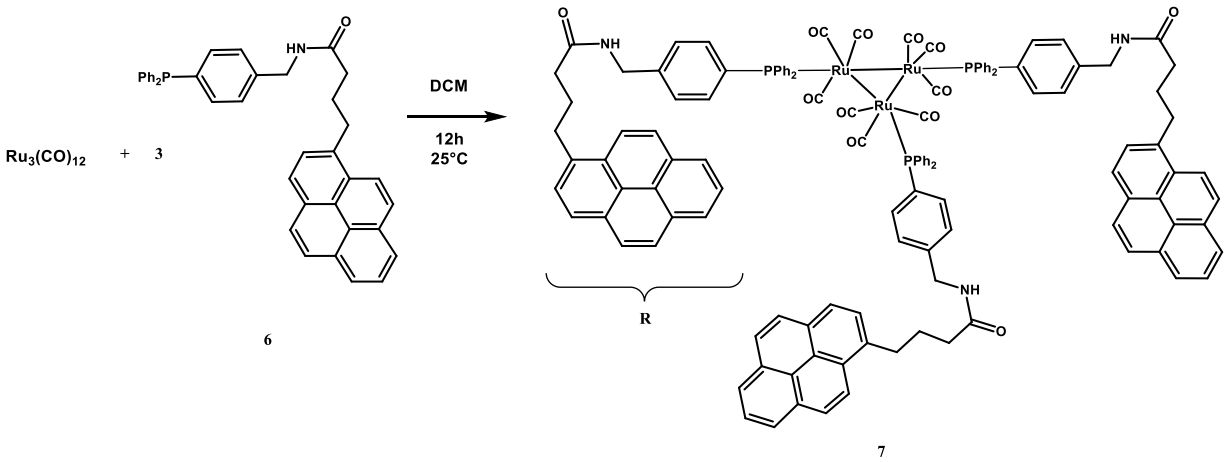

Fig. 3. Synthesis of ruthenium bifunctional compound 7.

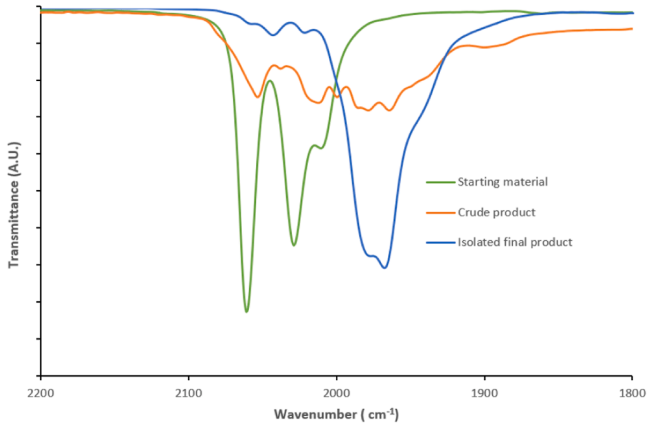

Fig. 4. IR spectra of starting material (green curve), crude product (orange curve) and the isolated trisubstituted product (blue curve).

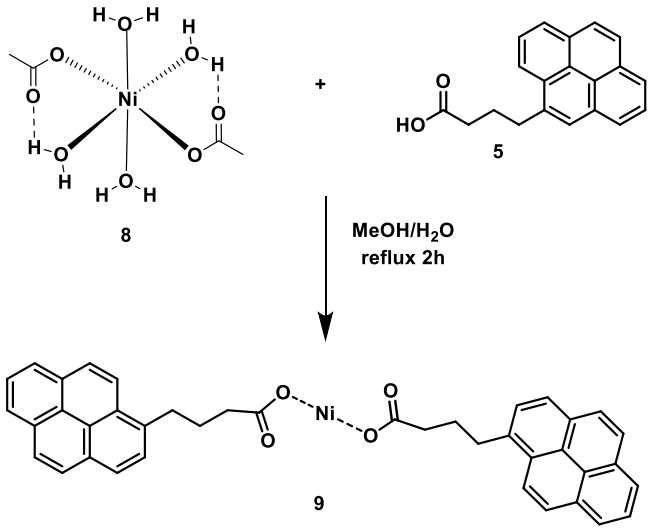

Fig. 5. Reaction between nickel acetate and 1-pyrenebutyric acid.

are coordinated in an unidentate mode with 2 ligands to 1 metal ratio (Fig. 5).

$Ni(cod)_2$ is used for the synthesis of the second nickel compound. Ni $(cod)_2$ is a 18-electron complex, which found a particular use as pre-catalyst in homogeneous catalysis [33]. Its π- acceptor alkene cyclooctadiene (cod) ligands stabilize low-valent Ni but can be easily displaced by strong σ-donors such as phosphine ligands. Therefore, the pyrene ligand **6** was added to $Ni(cod)_2$, and they were dissolved together in cold THF (−30 °C) to proceed with ligand exchanges. The cold bath was removed and 1 bar CO was then bubbled through the solution during one hour to provide extra carbonyl ligands as a replacement for cod. The reaction was then stirred during two hours at room temperature (Fig. 6).

The solvent was evaporated under reduced pressure and the solid was washed with cold pentane and then dissolved in DCM. A yellow solid appeared after evaporation of the solvent. The solid was characterized first of all by IR. Three peaks in the carbonyl region at 2069, 1999 and 1938 cm^{-1} (Fig. 7) confirm the presence of CO ligands. The carbonyl peaks are in accordance with the literature. Two kinds of reported compounds give similar carbonyl stretching bands: 2065 (A_1), 1980 (E modes) for tricarbonyls and 1995 (ν_{sym}) and 1920 (ν_{asym}) for dicarbonyls [34]. The quantity of carbonyl stretching bands of our synthetized compound lets us think that there is a mixture of dicarbonyl and tricarbonyl products (Fig. 7). The TLC indeed shows two spots that confirms this hypothesis about a mixture of mono- and di-substituted products (Fig. S11). The ^{31}P NMR shows three peaks at 32.24, 30.73, 28.87 ppm. The position of phosphorus peaks shifted to higher values, compared to free phosphine ligand ($\delta = -6$ ppm) confirming the exchange of phosphine ligand with metallic core (Fig. S12). The ^{1}H NMR confirms the presence of the aromatic entity (8.3–7.3 ppm) (Fig. S13). The synthetized nickel compound **11** will be used as a mixture for the functionalization of GNPs.

The last metallic compound synthetized is the iron precursor. $Fe(CO)_5$ was used as starting material in this synthesis. Controlling the degree of substitution of iron pentacarbonyl with neutral ligands is usually very difficult [35]. Moreover, selective formation of only one substitution product is labored, since there are separation difficulties for mono- from di-substituted product, as well as the excess of the free ligand from the products. The monosubstituted complex $Fe(CO)_4PPh_2R$ can be made from $Fe(CO)_5$ only under very specific conditions like, either in combination with the photochemical and thermal procedure [36], or using metal hydrides [37], or using catalysts such as cobalt salt [38] or carbonyl anions [39]. The di-substituted product is more difficult to obtain and the best initial procedure reported by Siegl was the reaction of $Fe(CO)_5$ with $LiAlH_4$ for 50 h in the presence of an excess in THF under reflux [37]. This synthetic approach was tested here with the pyrene ligand and should make it possible to synthesize only one product by reacting iron (0) pentacarbonyl with aluminum lithium hydride ($LiAlH_4$) in THF in the presence of our neutral ligand to produce a large quantity of $Fe(CO)_3(PPh_2R)_2$. The ^{31}P NMR shows several phosphorus peaks (Fig. S14) and the IR spectrum of the product indicates

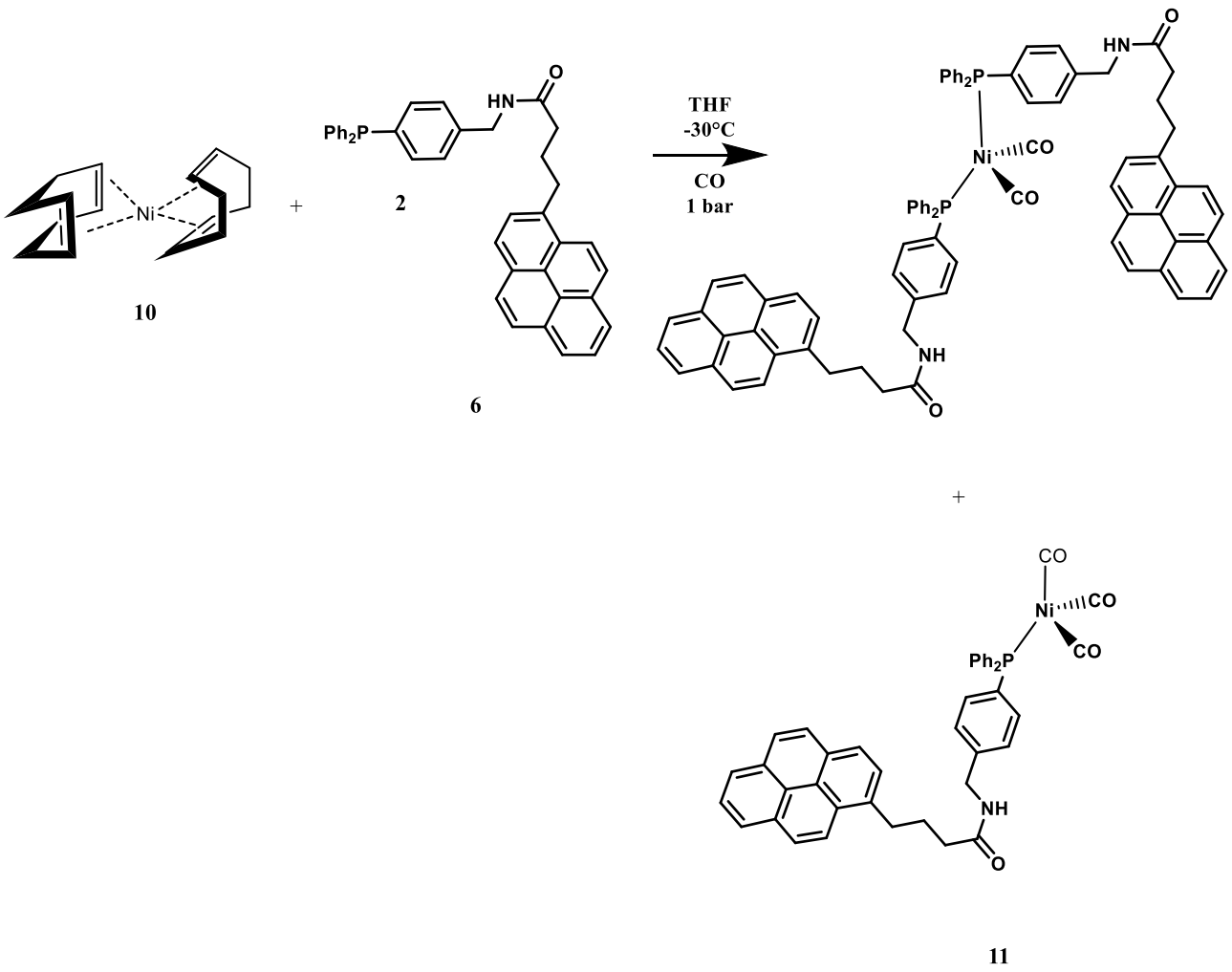

Fig. 6. Synthesis of nickel bifunctional compound 11.

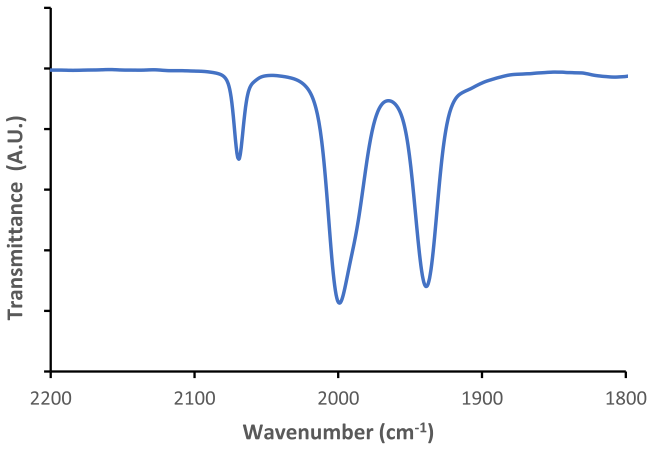

Fig. 7. Carbonyl region IR spectrum of nickel compound 11.

that, despite the number of equivalents respected during the procedure, a mixture of products was obtained (Fig. S15). As the synthesis of Siegl did not give us only one di-substituted product, we turned on to another synthesis proposed by Brunet et al. [40], as a simple and effective method to obtain the desired product **13** (Fig. 8).

The reaction of $Fe(CO)_5$ and KOH gives a product, $KHFe(CO)_4$, that can react with a phosphine ligand and give a single product, that of disubstitution. A downfield shift of phosphorus peak (^{31}P NMR $\delta = 82$ ppm) confirms that the reaction took place, compared to the free phosphine ligand ($\delta = -6.07$ ppm) (Fig. S16). IR spectrum shows, in the carbonyl stretching region, a distinct shift of CO stretching bands towards smaller wavenumbers confirming the exchange of CO for phosphine ligands (Fig. 9).

The IR peak at 1876 cm^{-1} is a characteristic peak of disubstituted product, in correspondence with the literature [35]. The analysis of the compound by HRMS reveals the intact compound (*m/z* 1262.36) (Fig. S17). This pure and perfectly identified iron compound (Brunet product **13**) will be used for the functionalization of graphene in the subsequent steps.

3.3. Immobilization of metallic precursors on graphene nanoplatelets (GNPs)

The pyrene group is important in this work for non-covalent immobilization of precursors on the surface of GNPs. The pyrene and graphene are lipophilic, so we need to use polar solvents to ensure optimal π-π stacking during the immobilization step [11,25]. We used dichloromethane for the immobilization of ruthenium (**7**), nickel (0) (**9**), nickel (II) (**11**) and iron (**13**) compounds according to their solubility. First, 100 mg of GNPs were dispersed in DCM in an ultrasonic bath for 45 min. The metallic compounds **7, 9, 11** and/or **13** were dissolved in small quantity of DCM, and added to the dispersed GNPs. The mixtures were stirred for 60 min at room temperature [25,41]. After stirring, the mixtures were filtrated (PVDF 0.45 μm) to separate the functionalized

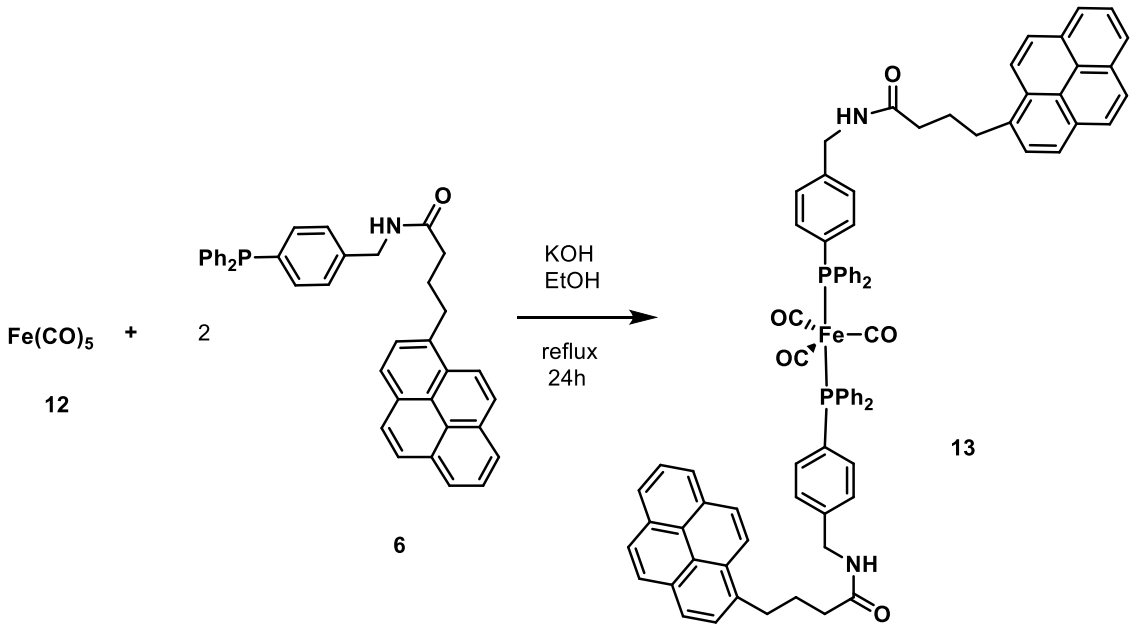

Fig. 8. Synthesis of Brunet adapted to our case to obtain iron/pyrene compound 13.

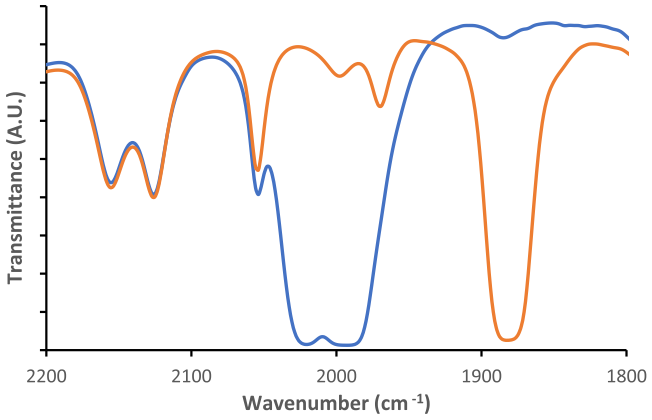

Fig. 9. IR spectra of Fe $(CO)_5$ starting material 12 (blue curve) and final disubstituted product 13 (orange curve).

GNPs from the liquid phase. The liquid phase was evaporated and the residue left was weighed to quantify the quantity of non-immobilized metal compound. By taking the difference between the initially introduced quantity and the one recovered after evaporation of the liquid phase, we can calculate the quantity of metal immobilized on GNPs. The solids were then pyrolyzed at two different temperatures, namely 400 °C and 600 °C under inert atmosphere (Ar/H_2 95/5) during one hour. This thermal treatment is required to remove carbonyl ligands surrounding the metal and the bifunctional ligand used to immobilize them on the support in order to obtain just a metallic core on the surface of graphene nanoplatelets. Since the properties of nanoparticles are dependent on their size, the possibility to prepare them with a narrow distribution on the surface of the chosen support is very important [42]. The use of higher activation temperatures can damage the graphene nanoplatelets structure [41], what is in contrast with our non-covalent strategy of metal anchoring on the substrate. Moreover, high temperatures promote the formation of bigger nanoparticles, so, the best activation temperature has to be investigated [43,44].

3.4. Characterization of Ru, Ni and Fe catalysts

Different mono- and bi-metallic catalysts were prepared by varying the combination of pyrene-tagged compounds immobilized on the GNP surface: Ru, Ni, Fe, Ni-Ru, Fe-Ru and Ni-Fe. Our strategy presents the major advantage of allowing bimetallic materials to be prepared as easily as monometallic ones in a single step, by simply dissolving together two different pyrene-tagged compounds in a single solution. This will ensure intimate contact between the two metals.

ICP analyses are necessary to determine the exact metal loading in the thermally-activated GNPs based catalysts, especially in the case of bimetallic combinations (Table 1). Different metal loadings between 0.3 and 3 wt% were obtained by varying the engaged quantities of precursors in the syntheses. This will also allow us to compare this important parameter in the catalytic tests. We can also see from Table 1, that for the majority of catalysts, there is still phosphorus left on the GNPs after the thermal activation. This is not a drawback as phosphide phases are catalytically-active for the conversion of glucose (from cellulose)

Table 1
Metals and phosphorus weight loadings of prepared catalysts: Ru, Ni (II), Ni (0), Ni(0)-Ru, Ni(II)-Ru, Fe, Fe-Ru, Ni(II)-Fe on GNPs, activated at 400 °C or 600 °C.

Entry	Metal M_1-M_2*	Metal loading ICP (wt%) Ru	Ni	Fe	P	Ratio M_1/M_2*
Cat-1**	Ru	0.3			/	
Cat-2**	Ru	2.4			0.78	
Cat-3	Ru	1.16			/	
Cat-4	Ru	3.03			0.86	
Cat-5	Ru	2.23			0.6	
Cat-6	Ni (II)		7.1			
Cat-7	Ni (0)		12.63		2.41	
Cat-8	Ni (0)-Ru	0.76	1.2		0.55	1.6
Cat-9	Ni (II)-Ru	0.65	1.04		0.42	1.6
Cat-10	Ni (II)-Ru	1.02	1.94		0.39	1.9
Cat-11	Ni (II)-Ru	0.96	2.88		0.3	3
Cat-12	Fe			10.65	1.91	
Cat-13	Fe-Ru	0.87		0.75	0.72	1
Cat-14	Fe-Ru	0.5		0.92	0.62	2
Cat-15	Fe-Ru	1.56		0.5	0.5	0.32
Cat-16	Ni (II)-Fe		3.46	0.66	0.32	5

*M_2 = Ru (entry 8–11 and 13–15) and M_2 = Fe in the case of Ni-Fe (entry 16), ** = activated at 400 °C.

into sorbitol under mild conditions (150 °C, 8 h, 5 MPa H_2) with 87% of yield [45].

The chemical state of metals and the presence of other elements on the surface of GNPs were evaluated by XPS. Let us, first, analyze the nickel catalysts, which were synthetized from the nickel zero precursor **11**: Ni (0)/GNP (Cat-7 Table 1) and Ni(0)-Ru/GNP (Cat-8 Table 1). The XPS spectra show the presence of Ni 2p and P 2p peaks (Fig. 10). Ni was detected in GNP catalyst with 2.9 at.% and P was detected with 0.9 at.%. O 1 s, N 1 s and C 1 s were detected also in the composition (Fig. S18). The core level spectrum P 2p shows the presence of phosphate and phosphide phases thanks to two P 2p doublet contributions measured with P $2p_{3/2}$ binding energies of 134 eV and 130.3 eV, respectively [46]. The presence of phosphide (130.3 eV) lets us think that a phosphide nickel phase is formed. The core level spectrum Ni $2p_{3/2}$ shows the presence of Ni_xP_y at 852.7 eV and Ni $^{2+}$at 856.3 eV and a shake-up satellite at 861.0 eV [47]. However, the metallic phase of nickel (Ni 0) and nickel phosphide phase (Ni_xP_y) have the same binding energy and the metallic phase can also be present. The oxidized nickel phase formation can be explained by the storage of the catalyst and its direct interaction with air.

A mixture of nickel phosphate and nickel phosphide is observed for two types of catalysts, mono- and bimetallic one (Cat-7 and Cat-8 Table 1), which is in accordance with the synthetic way of preparation of these catalysts. In both cases the pyrene bifunctional ligand **6** plays the role of the precursor and brings phosphorus on the surface of GNPs. When comparing monometallic with bimetallic formulation, we observe

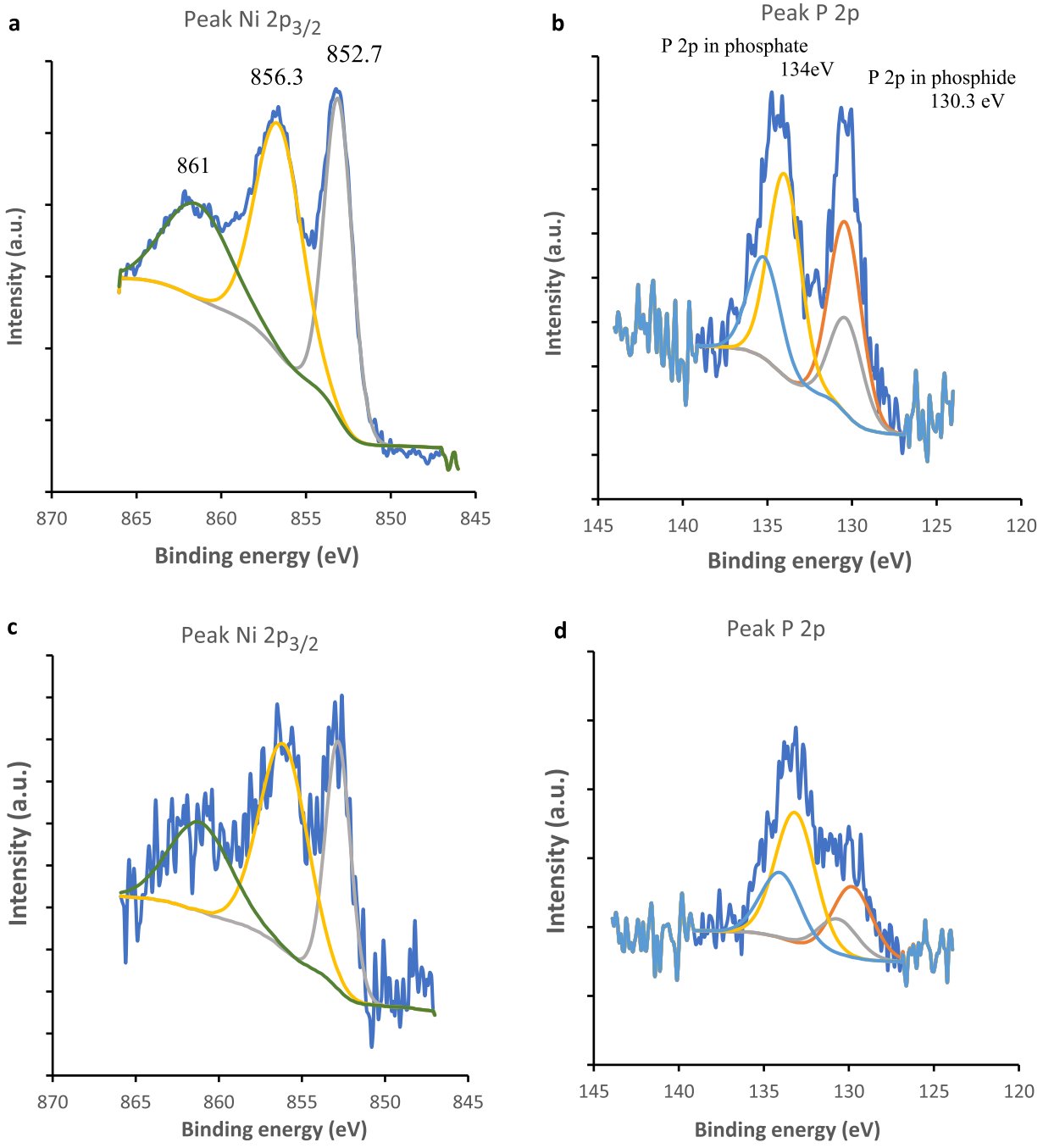

Fig. 10. Fitted XPS spectra of Ni (0)/GNP catalyst (Cat-7) : (a) Ni $2p_{3/2}$ spectrum (b) P 2p spectrum and Ni (0)-Ru/GNP (Cat-8) (c) Ni $2p_{3/2}$ spectrum (d) P 2p spectrum.

that a higher proportion of nickel phosphide is present in the monometallic one.

As for the nickel catalysts prepared from the Ni (II) precursor **9**, Ni (II)/GNP (Cat-6) and Ni (II)-Ru/GNP (Cat-9) were compared: the XPS spectra show a mixture of Ni^{2+} at 858.6 eV and Ni (0) situated at 852.5 eV. The mixture of oxidized and non-oxidized phase is detected. The thermal treatment reduces the nickel precursor partially, but, despite the treatment, the oxidation takes part very fast for the non-noble metal, regarding the conditions of the storage in air (Fig. S19). For all ruthenium catalyst, ruthenium is reduced to its zero-oxidation state (Fig. S20). In the case of iron catalysts Fe/GNPs and Fe-Ru/GNPs, the XPS analysis shows the presence of iron oxide in both catalysts (Figs. S21, S22). Despite the synthetic strategy involving an iron (0) precursor, iron seems to be oxidized after the thermal activation under inert atmosphere (Ar/H_2). This is very common with non-noble metals as all transfer steps and the storage were done in the air. Finally, the bimetallic catalyst Ni (II)-Fe/GNPs (Cat-16) presents a mixture of oxidized nickel and iron; and non-oxidized nickel (Fig. S23).

Regarding surface amount in each element analyzed at the surface (Tables S1, S2), we can see that in the case of the monometallic Ru/GNP catalyst, the atomic percentages calculated from XPS spectra are in accordance with the weight percentage from ICP analysis: the atomic percentages increase with the weight of the metal (from Cat-3 to Cat-5). However, for the bimetallic catalysts that contain ruthenium (Cat-8 to Cat-11 and Cat-13 to Cat-15), the atomic percentages of ruthenium are between 0.1 and 0.2 at.% and are difficult to corroborate with those obtained from ICP analysis. This is due to subtle surface effects that can occur with bimetallic nanoparticles, such as surface segregation driven by lower surface energy, formation of alloys if the two metals are miscible, surface oxidation if one metal (here Fe for example) is more easily oxidized *etc*. In particular, in the case of Fe-Ru bimetallic systems, it is known from phase diagrams that these metals are very miscible and will form solid solutions [48]. By contrast, Ru-Ni are immiscible and prefer separated pure phases [49]. In addition, particle size will also influence percentages of metal detected by XPS analysis, as the depth of XPS analysis is ~5 nm so larger particles will not contribute fully to the XPS at.% detected on the surface. The wt% determined by ICP is by opposition a bulk analysis.

For monometallic nickel catalysts (Cat-6 and Cat-7), the atomic percentage increases with the metal loading, but it is not corroborated for the bimetallic ones (Cat-8 to Cat-11). As for bimetallic iron catalysts (Cat-13 to Cat-15), the atomic percentage is the same in the three catalysts, despite the different weight metal loadings. For the last bimetallic catalyst Ni (II)-Fe (Cat-16), the atomic percentages of both metals are in accordance with other values for all catalysts (around 0.14 at.%). These effects can be explained by all arguments developed above for Ru that cannot be disentangled here.

The catalysts were then characterized by powder X-ray diffraction. The XRD diffraction pattern obtained for the ruthenium catalyst is the same as for GNPs alone, no peak of ruthenium was detected (**Figs. S24, S25**) indicating the amorphous nature of the nanoparticles or their very small sizes. The nickel phosphide and nickel metallic phases were detected by XRD in the bimetallic catalysts (Ni (0)-Ru/GNP, Cat-8), in accordance with XPS analysis (Fig. 11). The XPS peak at 852.5 eV contains, probably the mixture of the two species, metallic nickel and nickel phosphide Ni_xP_y. As for Ni (II)/GNP catalyst, the metallic nickel phase was also detected (Fig. S26).

TEM images were taken for each type of catalyst (Figs. 12, S27 and 28). For ruthenium catalyst activated at 600 °C, the particles are small (under 10 nm) and well dispersed (Fig. 12A, B). The absence of peaks in the XRD diffraction pattern, compared to the pristine GNPs XRD diffraction pattern, can therefore be explained by the small size of the ruthenium particles. For Ni (II)/GNP catalyst, particles between 10 and 12 nm and well dispersed were observed (Fig. 12C, D). In the case of bimetallic Ni (II)-Fe/GNP catalyst, the particles are smaller than Ni (II)/GNP (Fig. 12E, F). the biggest particles are obtained for the Ni (0)/GNP, around 20 nm (Fig. 12G, H). In the case of other formulations, Fe/GNP and Fe-Ru/GNP (Figs. S25 and 26), the particles are small (under 10 nm), like in the case of Ru/GNPs. We can see that the functionalization with pyrene ligand as precursor gives a homogeneous dispersion of small nanoparticles for each type of metallic catalyst.

3.5. *Catalytic activity in the reaction of glucose hydrogenation into sorbitol*

The characterized catalysts were tested in the reaction of hydrogenation of glucose into sorbitol under H_2 (30 bar pressure, 1700 rpm stirring rate). First catalytic tests were performed at 140 °C during 6 h under 30 bar H_2 with 1 g of glucose and 30 mg catalyst with the monometallic Ru/GNPs catalysts (Table 2).

These first experiments let us to choose the activation temperature in the idea to improve the sorbitol selectivity and conversion of glucose. We see that if the catalyst is activated at 600 °C (Table 2), the selectivity in sorbitol increases, as well as conversion and yield. 1.16 wt% in ruthenium (Cat-3) activated at 600 °C gives nearly the same result than 2.4 wt% Ru activated at 400 °C. A higher activation temperature allows to divide the amount of noble metal by two for getting the same performance. When increasing the loading to 3 wt% of ruthenium (Cat-4), the catalyst converts nearly all glucose and gives a high selectivity for sorbitol. In view of these results, all the other prepared catalysts were activated at 600 °C. For the next catalytic tests, we adapted the reaction conditions to the catalysts' nature. All subsequent tests being carried out with materials based on non-noble metals, known to have problems of leaching and deactivation after recycling [18], the quantity of catalyst was increased (60 mg), the quantity of glucose was decreased (500 mg), while the reaction temperature was increased up to 160 °C. However, in order to be able to compare the performance, the time of reaction was reduced from 6 to 2 h.

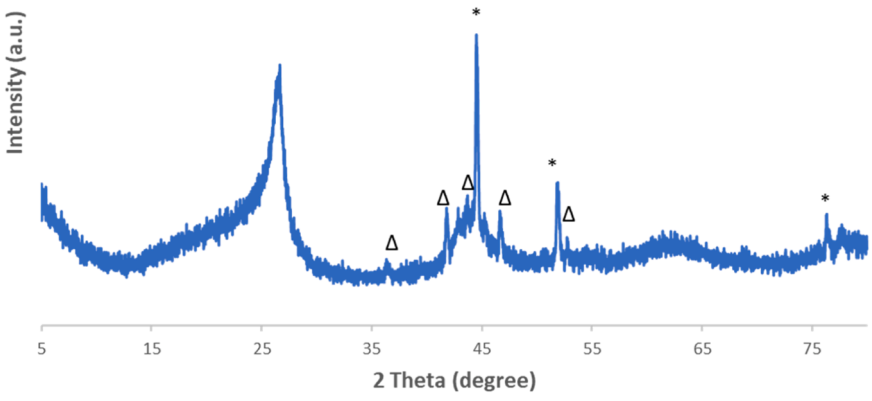

Fig. 11. Powder X-ray diffraction patterns of Ni (0)-Ru /GNPs (entry 15 in Table 1). * = metallic nickel Δ = nickel phosphide.

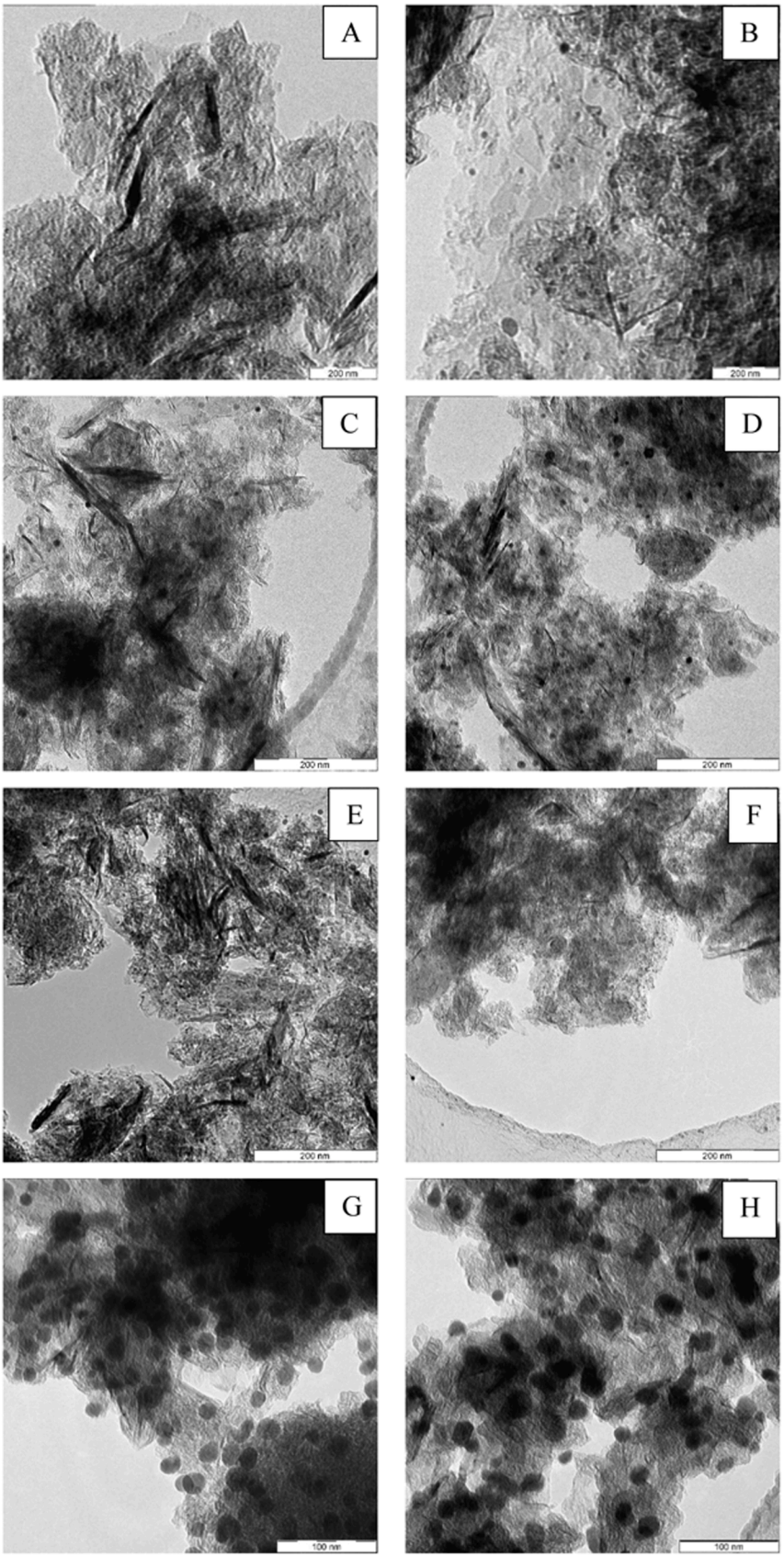

Fig. 12. TEM images of Ru/GNP (Cat-4) (A, B); Ni (II)/GNP(Cat-6) (C, D); Ni (II)-Fe/GNP (Cat-16) (E, F); Ni (0)/GNP (Cat-7) (G, H) catalysts after thermal activation at 600 °C.

Table 2
Hydrogenation of glucose into sorbitol over ruthenium supported catalysts at 140 °C under 30 bar H_2 during 6 h.

	Activation temperature (°C)	Loading (wt% ICP)	Conversion (%)	Sorbitol selectivity (%)	Sorbitol yield (%)
Cat-1	400	0.30	63	5	3.15
Cat-2	400	2.40	42	64	26.88
Cat-3	600	1.16	47	69	32.43
Cat-4	600	3.03	93	86	79.98

The ruthenium (2.23 wt%) catalyst (Cat-5, Table 3) was tested under these new conditions and showed good results: 66% conversion of glucose and 74% selectivity in sorbitol after only 2 h of catalytic test. In comparison, 3.03 wt% (Cat-4) ruthenium gives a high conversion and a slightly higher selectivity in sorbitol but for a much longer reaction time (6 h) (Fig. 12A and Table 2).

Nickel monometallic catalysts prepared from the two Ni (II) and Ni (0) precursors were then tested (Cat-6 and Cat-7, Table 3): Ni (II)/GNP catalyst (Cat-6) with 7.1 wt% of nickel gives 27% of selectivity for sorbitol while the Ni (0)/GNP (Cat-7) that presented 12.63 wt% Ni gives only 15% selectivity.

In general, the catalytic reaction of glucose hydrogenation is quite selective but the formation of several by-products is possible [50]. Fructose is produced by isomerization of glucose which is catalyzed by leached metals Fe^{3+} and Ni^{2+}, which act as Lewis acids [51]. Mannitol is produced through hydrogenation of fructose and mannose [23]. Fructose, mannose and mannitol are the major by-products that were identified in the present work and can explain the low sorbitol selectivity in some cases.

Obviously, not only the metal loading plays a crucial role in the selectivity of the reaction, but there are other effects that have to be considered as chemical composition, metallic oxidation state and particle sizes. Indeed, the smaller particles observed in the case of Cat-6 (Ni (II)/GNP) give a better selectivity than Cat-7 (Ni (0)/GNP) with bigger ones (compare Figs. 12C, D and 13) [52].

In the case of bimetallic catalysts Ni-Ru, the conversion and the sorbitol selectivity increase when the quantity of nickel increases (we tested up to 3Ni:1Ru), to reach 60% conversion even with only 1 wt% ruthenium (Fig. 13B).

The bimetallic catalysts Fe-Ru/GNP show a high catalytic activity with a high loading in ruthenium (1Fe/3Ru, Fig. 13C). However, when increasing the quantity of iron the conversion is not enhanced, in accordance with its inactivity for the studied catalytic reaction (Fig. 13D). The monometallic iron catalyst gives the same conversion and selectivity compared to a blank test with only the GNPs support pretreated at 600 °C for 1 h (57% of conversion, 8% of sorbitol selectivity and 4.5% of sorbitol yield).

We then tried to remove completely the expensive (yet very active) noble metal ruthenium in a bimetallic combination, and tested Ni-Fe/GNP. When comparing the sorbitol selectivity for the monometallic nickel catalyst with 7.1 wt% Ni and the catalyst Ni (II)-Fe/GNP (3.46–0.66 wt% in Ni and Fe, respectively), we see that the bimetallic catalyst has better selectivity: 40% compared to 15% for the monometallic catalyst. Moreover, this enhancement occurs despite the low total loading in nickel and iron (4.12 wt% for the two metals) (Fig. 13D). This indicates a synergetic effect between the two metals, as the bimetallic material present catalytic results that outperforms the sum of those of the monometallic ones.

This result can be explained by different phenomena, the first one being particle sizes. In the bimetallic catalyst, the particles are very small while in the case of the corresponding monometallic nickel catalyst, the particles are around 20 nm (Fig. 12). It has been shown that the particle size plays an important role in catalytic reactions, better catalytic tests results being usually obtained with smaller particles, and especially in this transformation [43]. The other point is the positive effect of iron on nickel catalysts that was observed and developed in the literature [22,53]. Indeed, Gallezot et al. [21] and Court et al. [22] showed that iron is a promoter for nickel based catalysts of Raney-Ni type. Synergy effect between iron and nickel in an alloy structure prepared by a sol-gel method was also recently demonstrated by Fu et al. [23].

When comparing with bimetallic catalysts based on ruthenium (Fe-Ru and Ni-Ru), the selectivity to sorbitol is almost the same for 0.76 wt% and 0.5 wt% of ruthenium (Table 4). Even a small quantity of ruthenium is already enough to get around 50% of sorbitol selectivity. These results agree with literature. Frecha et al. demonstrated that the addition of Ni is not justified in the case of Ni-Ru (3:0.5 wt%), as a 0.3 wt% of Ru is enough to completely hydrogenate the sugars by itself [53] . Here we obtained similar performance with a bimetallic catalyst based on non-noble metals, and totally devoid of ruthenium (Table 4).

4. Conclusion

We have reported an original method for graphene nanoplatelets functionalization by a non-covalent way without altering their aromatic network, by introducing on their surface a bifunctional ligand bearing a pyrene ligand and a metallic entity. Three metallic compounds were synthesized by ligand exchange from Ru, Ni and Fe reactants, and their molecular entity confirmed by detailed characterization. In addition, a Ni (II) compound was obtained from 1-pyrenebutyric acid. These new metal/pyrene synthesized compounds where introduced at the surface of GNPs by π-π stacking and thermally treated to remove the organic parts. The pyrene group has demonstrated its efficiency in giving high dispersion of nanoparticles and avoiding sintering on GNPs during the thermal treatment of the metal precursors.

The so-prepared catalysts were fully characterized and studied in the catalytic reaction of glucose hydrogenation. Ruthenium supported on graphene nanoplatelets (3.03 wt%) shows the best selectivity in the catalytic reaction, with 92% of conversion and 87% of selectivity in sorbitol within 6 h. Non-noble metals such as nickel and iron are, in turn, far less active, with 60% of conversion in both cases and around 15% of selectivity in the case of nickel and only 4% of selectivity in the case of iron. However, nickel is known as being efficient for this type of reaction, but only in bulk form as Raney nickel. The addition of ruthenium in the nickel catalyst showed an enhancement in the catalytic activity. Only 0.5 wt% of ruthenium is enough to get nearly 50% sorbitol selectivity. On the contrary, iron decreases the activity of ruthenium as it is inactive for the hydrogenation of glucose into sorbitol. More

Table 3
Hydrogenation of glucose into sorbitol over ruthenium supported catalysts at 160 °C under 30 bar H_2 during 2 h.

	Metal	Loading (wt% ICP)	Conversion (%)	Sorbitol selectivity (%)	Sorbitol yield (%)
Cat-5	Ru	2.23	66	74	48.84
Cat-6	Ni (II)	7.1	50	27	13.5
Cat-7	Ni (0)	12.63	61	15	9.15
C at-12	Fe	10.65	62	4	2.48

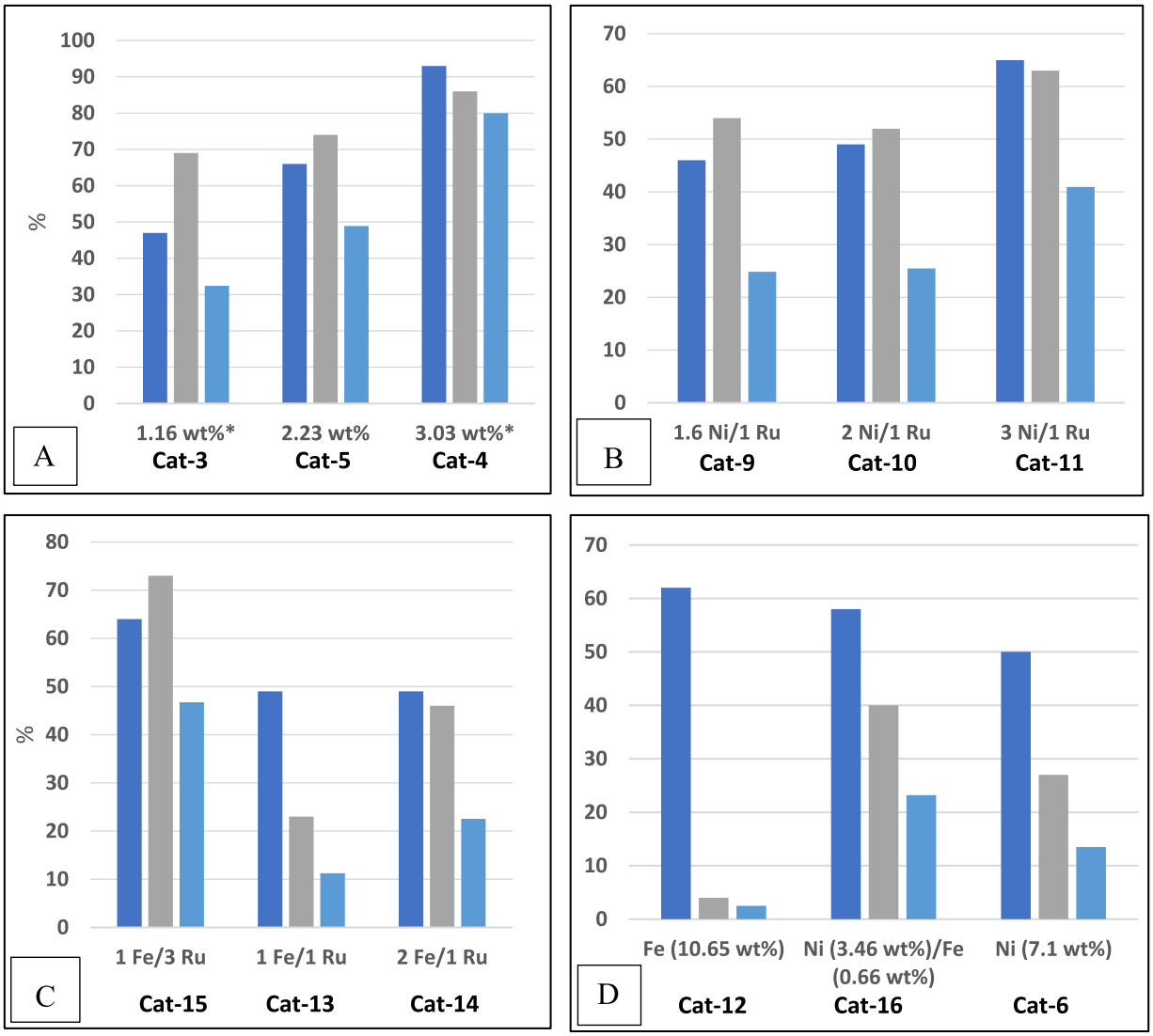

Fig. 13. A: Conversion (blue), sorbitol selectivity (gray) and sorbitol yield (light blue) in function of ruthenium loading on GNPs (*catalytic test conditions: 30 bar H_2, 140 °C, 6 h, 1 g of glucose, 30 mg of catalyst). B: Results of catalytic tests in function of the metallic weight ratio Ni:Ru on GNP. C: Results of the catalytic tests in function of the metallic weight ratio Fe:Ru on GNP. D: Results for catalytic tests with non-noble metals, Fe, Ni and their mixture. Catalytic test conditions: 30 bar H_2, 160 °C, 2 h, 0.5 g of glucose, 60 mg of catalyst.

Table 4
Hydrogenation of glucose into sorbitol over bimetallic catalysts tested at 160 °C under 30 bar H_2 during 2 h.

	Metals	Loading (wt%, ICP)	Weight ratio calculated from ICP	Conversion (%)	Sorbitol selectivity (%)	Sorbitol yield (%)
Cat-8	Ni-Ru	1.2/0.76	1.6/1	46	48	22.1
Cat-14	Fe-Ru	0.92/0.5	2/1	49	46	22.5
Cat-16	Ni-Fe	3.46/0.66	5/1	58	40	23.2

interestingly, the promoter effect of iron in nickel catalysts was demonstrated with 58% of conversion and 40% of selectivity obtained for 4.12 wt% in both metals in a bimetallic Fe-Ni formulation, demonstrating a synergetic effect. This allows to obtain interesting catalytic performance with a supported catalyst devoid of noble metal. Higher weight percentage in non-noble metals can enhance the selectivity in sorbitol and conversion of glucose, so there is still room for improvement, also by optimizing parameters of the catalytic reaction. But this latter aspect was not the objective of the present contribution. We herein demonstrated the versatility of our synthetic approach to easily obtain a wide range of compositions, sizes and loadings of GNPs-supported nanoparticles allowing pertinent comparisons for sugar catalysis that could easily be extended to other systems (other metals, other carbon supports, or other sugar molecules), with important implications for biomass valorization processes.

CRediT authorship contribution statement

Nadzeya Kryvutsa: Methodology, Investigation, Formal analysis, Validation, Visualization, Writing – original draft. **Pierre Eloy:** Investigation, Formal analysis, Validation, Visualization, Writing – review & editing. **Benoit Hackens:** Writing – review & editing, Supervision. **Sophie Hermans:** Conceptualization, Methodology, Validation, Writing – review & editing, Funding acquisition, Project administration,

Supervision.

Declaration of Competing Interest

The authors declare that they have no known competing financial interests or personal relationships that could have appeared to influence the work reported in this paper.

Data availability

Data will be made available on request.

Acknowledgments

The authors gratefully thank the Fonds de la Recherche Scientifique (F.R.S.-FNRS – B.H. and S.H. are respectively senior research associate and research director with F.R.S.-FNRS) and Université Catholique de Louvain (Belgium) for funding. We thank also Jean-François Statsyns for technical support, François Devred for XRD analyses and Laurent Collard for HPLC technical assistance.

Supplementary materials

Supplementary material associated with this article can be found, in the online version, at doi:10.1016/j.mcat.2023.113222.

References

[1] K.S. Novoselov, et al., Electric field effect in atomically thin carbon films, Science 306 (2004) 666–669.
[2] E. Morales-Narváez, L.F. Sgobbi, S.A.S. Machado, A. Merkoçi, Graphene-encapsulated materials: synthesis, applications and trends, Prog. Mater. Sci. 86 (2017) 1–24.
[3] E. Pop, V. Varshney, A.K. Roy, Thermal properties of graphene: fundamentals and applications, MRS Bull. 37 (2012) 1273–1281.
[4] Shahriary Leila, A. Athawale Anjali, Graphene oxide synthesized by using modified hummers approach, Int. J. Renew. Energy Environ. Eng. 02 (2014) 58–63.
[5] S. Gadipelli, Z.X. Guo, Graphene-based materials: synthesis and gas sorption, storage and separation, Prog. Mater. Sci. 69 (2015) 1–60.
[6] K.M. Yam, N. Guo, Z. Jiang, S. Li, C. Zhang, Graphene-based heterogeneous catalysis: role of graphene, Catalysts 10 (2020) 53–70.
[7] V. Georgakilas, et al., Noncovalent functionalization of graphene and graphene oxide for energy materials, biosensing, catalytic, and biomedical applications, Chem. Rev. 116 (2016) 5464–5519.
[8] C.W. Lai, Graphene composites, Diffus. Found. 23 (2019) 57–63.
[9] V. Georgakilas, et al., Functionalization of graphene : covalent and non- covalent approaches, derivatives and applications functionalization of graphene : covalent and non-covalent approaches, derivatives and applications, Chem. Rev. 112 (2012) 6156–6214.
[10] C. Peng, X. Zhang, Chemical functionalization of graphene nanoplatelets with hydroxyl, amino, and carboxylic terminal groups, Chemistry 3 (2021) 873–888 (Easton).
[11] C. Janiak, A critical account on n-n stacking in metal complexes with aromatic nitrogen-containing ligands, J. Chem. Soc. Dalton Trans. (2000) 3885–3896, https://doi.org/10.1039/B003010O.
[12] A.M. Ruppert, K. Weinberg, R. Palkovits, Hydrogenolysis goes bio: from carbohydrates and sugar alcohols to platform chemicals, Angew. Chem. Int. Ed. 51 (2012) 2564–2601.
[13] V. Balan, Current challenges in commercially producing biofuels from lignocellulosic biomass, ISRN Biotechnol. 2014 (2014) 1–31.
[14] G.W. Huber, S. Iborra, A. Corma, Synthesis of transportation fuels from biomass: chemistry, catalysts, and engineering, Chem. Rev. 106 (2006) 4044–4098.
[15] B. García, J. Moreno, G. Morales, J.A. Melero, J. Iglesias, Production of sorbitol via catalytic transfer hydrogenation of Glucose, Appl. Sci. 10 (2020) 1843–1855.
[16] B. Kusserow, S. Schimpf, P. Claus, Hydrogenation of glucose to sorbitol over nickel and ruthenium catalysts, Adv. Synth. Catal. 345 (2003) 289–299.
[17] L.S. Ribeiro, J.J. Delgado, J.J.M. Órfão, M.F.R. Pereira, Carbon supported Ru-Ni bimetallic catalysts for the enhanced one-pot conversion of cellulose to sorbitol, Appl. Catal. B Environ. 217 (2017) 265–274.
[18] A. Romero, A. Nieto-Márquez, E. Alonso, Bimetallic Ru:ni/MCM-48 catalysts for the effective hydrogenation of D-glucose into sorbitol, Appl. Catal. A Gen. 529 (2017) 49–59.
[19] J. Zhang, J.B. Li, S.Bin Wu, Y. Liu, Advances in the catalytic production and utilization of sorbitol, Ind. Eng. Chem. Res. 52 (2013) 11799–11815.
[20] J. Wisniak, R. Simon, Hydrogenation of glucose, fructose, and their mixtures, Ind. Eng. Chem. Prod. Res. Dev. 18 (1979) 50–57.
[21] P. Gallezot, P.J. Cerino, B. Blanc, G. Flèche, P Fuertes, Glucose hydrogenation on promoted raney-nickel catalysts, J. Catal. 146 (1994) 93–102.
[22] J. Court, J.P. Damon, J. Masson, P. Wierzchowski, Hydrogenation of glucose with bimetallic catalysts (NiM) of Raney type, Stud. Surf. Sci. Catal. 41 (1988) 189–196.
[23] Y. Fu, L. Ding, M.L. Singleton, H. Idrissi, S. Hermans, Synergistic effects altering reaction pathways: the case of glucose hydrogenation over Fe-Ni catalysts, Appl. Catal. B Environ. 288 (2021), 119997-120006.
[24] S. De, J. Zhang, R. Luque, N. Yan, Ni-based bimetallic heterogeneous catalysts for energy and environmental applications, Energy Environ. Sci. 9 (2016) 3314–3347.
[25] C. Vriamont, M. Devillers, O. Riant, S. Hermans, Catalysis with gold complexes immobilised on carbon nanotubes by π–π Stacking interactions: heterogeneous catalysis versus the boomerang effect, Chem. Eur. J. 19 (2013) 12009–12017.
[26] M. Nishimura, M. Ueda, N. Miyaura, Palladium-catalyzed biaryl-coupling reaction of arylboronic acids in water using hydrophilic phosphine ligands, Tetrahedron 58 (2002) 5779–5787.
[27] M.I. Bruce, et al., Cluster chemistry. Reactions between metal carbonyl clusters and Lewis bases initiated by radical ions: improved syntheses of substituted derivatives of M3and M4 clusters(M = Fe, Ru, Os or Co), J. Chem. Soc. Ser. Chem. Commun. (1982) 442–444, https://doi.org/10.1039/C39820000442.
[28] E. Alonso, D. Astruc, Introduction of the cluster fragment Ru3(CO)11 at the periphery of phosphine dendrimers catalyzed by the electron-reservoir complex [Fe(I)Cp(C6Me6)], J. Am. Chem. Soc. 122 (2000) 3222–3223.
[29] J. Lewis, D. Pippard, Preparation of undecacarbonyltriosmium derivatives 145 (1978).
[30] A.A. Isab, S. Ahmad, Complexation of (trimethylphosphine)gold(I) with selenones, Transit. Met. Chem. 31 (2006) 500–503.
[31] G.B. Deacon, R.J. Phillips, G. Deacon, R. Phillips, Relationships between the carbon-oxygen stretching frequencies of carboxylato complexes and the type of carboxylate coordination, Coord. Chem. Rev. 33 (1980) 227–250.
[32] E.G. Palacios, G. Juárez-López, A.J. Monhemius, Infrared spectroscopy of metal carboxylates: II. Analysis of Fe(III), Ni and Zn carboxylate solutions, Hydrometallurgy 72 (2004) 139–148.
[33] S.Z. Tasker, E.A. Standley, T.F. Jamison, Recent advances in nickel catalysis, Nature 509 (2015) 299–309.
[34] M. Marín, et al., Synthesis, structure and nickel carbonyl complexes of dialkylterphenyl phosphines, Chem. Eur. J. 25 (2019) 260–272.
[35] A.F. Clifford, A.K. Mukherjee, Iron carbonyl complexes of triphenylphosphine, triphenylarsine, and triphenylstibine, Inorg. Chem. 2 (1963) 151–153.
[36] H.L. Conder, M. York Darensbourg, The synthesis of group V substituted derivatives of iron pentacarbonyl in high yield, J. Organomet. Chem. 67 (1974) 93–97.
[37] W.O. Siegl, Mono-substitution of iron pentacarbonyl metal hydride: facilitation, J. Organomet. Chem. 92 (1975) 321–328.
[38] M.O. Albers, N.J. Coville, T.V. Ashworth, E. Singleton, The transition metal-catalysed reaction between Fe(CO)5 and group V donor ligands. A facile, high yield synthesis of Fe(CO)4PPh3, J. Organomet. Chem. 217 (1981) 385–390.
[39] S.B. Butts, D.F. Shriver, Mono-substitution of iron pentacarbonyl catalyzed by polynuclear iron carbonyl anions, J. Organomet. Chem. 169 (1979) 191–197.
[40] J.J. Brunet, F.B. Kindela, D. Neibecker, Expedient synthesis of (Ph 3 P) 2 Fe (CO) 3, J. Organomet. Chem. 368 (1989) 209–212.
[41] C. Vriamont, et al., Covalently and non-covalently immobilized clusters onto nanocarbons as catalysts precursors for cinnamaldehyde selective hydrogenation, J. Catal. 329 (2015) 389–400.
[42] C. Willocq, et al., Anchoring of Ru-Pt and Ru-Au clusters onto a phosphane-functionalized carbon support, Eur. J. Inorg. Chem. (2011) 4721–4729, https://doi.org/10.1002/ejic.201100384.
[43] S. Carlier, J. Gripekoven, M. Philippo, S. Hermans, Ru on N-doped carbon supports for the direct hydrogenation of cellobiose into sorbitol, Appl. Catal. B Environ. 282 (2021), 119515.
[44] W. Deng, X. Tan, W. Fang, Q. Zhang, Y. Wang, Conversion of cellulose into sorbitol over carbon nanotube-supported ruthenium catalyst, Catal. Lett. 133 (2009) 167–174.
[45] F. Mao, et al., Ru/P-containing porous biochar-efficiently catalyzed cascade conversion of cellulose to sorbitol in water under medium-pressure H2 atmosphere, Bull. Chem. Soc. Jpn. 93 (2020) 1026–1035.
[46] M. Streckova, et al., Nickel and nickel phosphide nanoparticles embedded in electrospun carbon fibers as favourable electrocatalysts for hydrogen evolution, Chem. Eng. J. 303 (2016) 167–181.
[47] Q. Zhang, et al., Ni-Phosphide catalysts as versatile systems for gas-phase CO2 conversion: impact of the support and evidences of structure-sensitivity, Fuel 323 (2022) 1–12.
[48] L.J. Swartzendruber, B. Sundman, The Fe-Ru (Iron-Ruthenium) system, Bull. Alloy Phase Diagr. 4 (1983) 155–160.
[49] H. Okamoto, Ni-Ru (Nickel-Ruthenium), J. Phase Equilibria Diffus. 30 (2009) 412.
[50] B. García, A. Orozco-Saumell, M. López Granados, J. Moreno, J. Iglesias, Catalytic transfer hydrogenation of glucose to sorbitol with raney Ni catalysts using biomass-derived diols as hydrogen donors, ACS Sustain. Chem. Eng. 9 (2021) 14857–14867.
[51] Y. Román-Leshkov, M. Moliner, J.A. Labinger, M.E. Davis, Mechanism of glucose isomerization using a solid lewis acid catalyst in water, Angew. Chem. Int. Ed. 49 (2010) 8954–8957.
[52] L.N. Ding, A.Q. Wang, M.Y. Zheng, T. Zhang, Selective transformation of cellulose into sorbitol by using a bifunctional nickel phosphide catalyst, ChemSusChem 3 (2010) 818–821.
[53] E. Frecha, D. Torres, A. Pueyo, I. Suelves, J.L. Pinilla, Scanning different Ni-noble metal (Pt, Pd, Ru) bimetallic nanoparticles supported on carbon nanofibers for one-pot cellobiose conversion, Appl. Catal. A Gen. 585 (2019), 117182.